Computation of three-dimensional flow around square and circular piers

Ming-Hseng Tseng[a],[*],[1], Chin-Lien Yen[b] and Charles C. S. Song[c]

[a] *Department of Information Management, Ling Tung College, Taichung, Taiwan*
[b] *Department of Civil Engineering and Hydrotech Research Institute, National Taiwan University, Taipei, Taiwan*
[c] *Department of Civil Engineering, St. Anthony Falls Laboratory, University of Minnesota, Minneapolis, MN, U.S.A.*

SUMMARY

The aim of the present study is to investigate, by numerical simulation, the three-dimensional turbulent flow field around square and circular piers. The numerical model employs a finite volume method based on MacCormack's explicit predictor–corrector scheme to solve weakly compressible hydrodynamic equations for turbulent flow. Computed results are compared with Dargahi's experimental measurements to assess the validity of the proposed model. Very good agreements are obtained. The results of flow simulation indicate that near the upstream face of the pier there exists a downflow, which joins the separated flow to form the horseshoe vortex stretched around the pier. This horseshoe vortex interacts with the wake vortex to create the upflow behind the pier. These phenomena appear to be very important to the mechanism of scouring around the pier. In general, the flow patterns for the square and circular piers are similar. However, the strengths of the downflow and horseshoe vortex are greater in the case of the square pier. The position of the horseshoe vortex around the circular pier is closer to the front face than that around the square pier. In the meantime, the domain of the wake flow in the case of the square pier is greater than that in the case of the circular one. Copyright © 2000 John Wiley & Sons, Ltd.

KEY WORDS: circular pier; downflow; horseshoe vortex; MacCormack's predictor–corrector scheme; square pier; three-dimensional flow; wake vortex

1. INTRODUCTION

Scouring is an important phenomenon in river mechanics. It generally takes place in alluvial channels, and around man-made structures, such as bridge piers and spur dikes. The latter normally is classified as local scour.

---

* Correspondence to: Department of Information Management, Ling Tung College, Taichung, Taiwan. Tel./fax: + 886 4 3861709.
[1] E-mail: mhtseng@mail.ltc.edu.tw

The flow of water around a pier on a channel bed is essentially three-dimensional and turbulent. This type of flow has many different aspects, which interact in a very complicated manner arising from the presence of the boundary layer in the approaching flow with the adverse pressure gradient set up by the pier, and resulting in a horseshoe vortex that occurs around the pier. In addition, there exist a downflow in the front side of the pier, a bow wave on the upstream free surface near the pier, and a wake vortex shedding in the downstream region behind the pier. The flow field is even more complex in the process of scouring. Even though a vast amount of experimental work on the problem of local scour around bridge piers (Breusers *et al*. [1], Ettema [2], Raudkivi and Ettema [3], Raudkivi [4], Melville and Sutherland [5]) exists, the three-dimensional turbulent flow field in this case is so complex that an accurate mathematical model is not yet available at this time.

Olsen and Melaaen [6] reported some results of a three-dimensional numerical computation of the flow and scour around a pier. The primary focus of their work was to propose a steady model for a particular case of very shallow water depth relative to the width of pier and, therefore, the results did not contain most of the complex features that are typical under general conditions. Furthermore, they only reported the downflow and the contraction flow near the cylinder, but the horseshoe vortex and the wake vortex were not well simulated.

Richardson and Panchang [7] applied a computational fluid dynamic (CFD) commercial code (FLOW-3D) to study the flow occurring at the base of a circular pier within a scour hole. However, in their study the equilibrium and the intermediate scour holes are assumed to be sections of a cone. Olsen and Kjellesvig [8] solved the Reynolds equations with the $k-\varepsilon$ turbulence model to estimate the maximum local scour depth around a circular pier, but their model only has first-order accuracy.

In most of the past studies, emphases have been placed upon the formulation of scour depth relations rather than the mechanism of scouring. The mechanism ought to be investigated in terms of the flow field and its significance in the process of scouring. The current authors have developed a three-dimensional transient flow model and a two-dimensional scour model for the investigation of the turbulent flow field and scouring around bridge piers (Yen *et al*. [9], Tseng [10]). By using such models, the flow field characteristics and the process of scouring around a square pier have been studied (Yen *et al*. [11]). The objective of the present study is to investigate, by numerical simulation, the pattern of the vortex system around the pier and the effect of pier shape, namely square and circular, on flow characteristics. The numerical model employs a finite volume method based on MacCormack's explicit predictor–corrector scheme to solve weakly compressible hydrodynamic equations, in which turbulent shear stress is represented by Smagorinsky's sub-grid scale turbulence model [12].

The contents of this paper are organized as follows. The numerical techniques employed to solve the three-dimensional transient weakly compressible hydrodynamic flow equations are presented first. Subsequently, the computation of flow around the circular pier is given to validate the proposed model using Dargahi's experimental data [13]. Then, the flow patterns for the square and circular piers are compared, which are also explored for an extension to describe the mechanism of scouring. Finally, the overall principal conclusions drawn from the study are summarized and presented in the last section.

2. NUMERICAL METHOD

2.1. Governing equations

For a weakly compressible hydrodynamic flow [14,15] in which the Mach number is very small, the equation of state may be represented by

$$p - p_0 = a_0^2(\rho - \rho_0) \tag{1}$$

where p is the pressure, a is the speed of sound, ρ is the density of fluid, and the subscript 0 refers to the reference condition. By substituting Equation (1) into the continuity and Navier–Stokes equations, one can obtain

$$\frac{\partial \boldsymbol{U}}{\partial t} + \frac{\partial \boldsymbol{E}}{\partial x} + \frac{\partial \boldsymbol{F}}{\partial y} + \frac{\partial \boldsymbol{G}}{\partial z} = 0 \tag{2}$$

where

$$\boldsymbol{U} = [p, \ \alpha u, \ \alpha v, \ \alpha w]^T$$

$$\boldsymbol{E} = \left[\kappa \alpha u, \ \alpha u^2 + \frac{p}{p_0} - \frac{\tau_{xx}}{\rho_0}, \ \alpha uv - \frac{\tau_{xy}}{\rho_0}, \ \alpha uw - \frac{\tau_{xz}}{\rho_0} \right]^T$$

$$\boldsymbol{F} = \left[\kappa \alpha v, \ \alpha uv - \frac{\tau_{yx}}{\rho_0}, \ \alpha v^2 + \frac{p}{p_0} - \frac{\tau_{yy}}{\rho_0}, \ \alpha vw - \frac{\tau_{yz}}{\rho_0} \right]^T$$

$$\boldsymbol{G} = \left[\kappa \alpha w, \ \alpha uw - \frac{\tau_{zx}}{\rho_0}, \ \alpha vw - \frac{\tau_{zy}}{\rho_0}, \ \alpha w^2 + \frac{p}{p_0} - \frac{\tau_{zz}}{\rho_0} \right]^T$$

$$\alpha = 1 + \frac{p - p_0}{\rho_0 a_0^2} = 1 + C_p M^2/2$$

and $\kappa = \rho_0 a_0^2$. T represents the transpose of the matrix; u, v, and w are the x, y, and z components of velocity respectively; x, y, and z are the longitudinal, transverse, and vertical co-ordinates respectively; τ_{xx}, τ_{xy}, τ_{xz}, ... represent the shear stress components; C_p is the pressure coefficient; and M is the Mach number. Since $M \ll 1$ for the present study, the coefficient α is set equal to 1.

2.2. LES turbulence model

For turbulent flow, the shear stress τ_{ij} is expressed as

$$\tau_{ij} = (\tau_{ij})_\ell + (\tau_{ij})_t \tag{3}$$

where subscripts ℓ and t stand for the laminar and turbulent parts respectively. The indices $i = 1, 2, 3$ and $j = 1, 2, 3$. The cell-averaged sub-grid scale (SGS) turbulence model due to Smagorinsky [12] is adopted for $(\tau_{ij})_t$ as follows:

$$\left(\frac{\tau_{ij}}{\rho_0}\right)_t = K\left(\frac{\partial u_i}{\partial x_j} + \frac{\partial u_j}{\partial x_i}\right) \tag{4}$$

and

$$K = (C\nabla_S)^2(2S_{ij}S_{ij})^{1/2} \tag{5}$$

in which $C = C_S[1 - \exp(-z^+/26)]$; $z^+ = zu^*/v$, where z is the distance from the center of the cell adjoining the bed, u^* is the shear velocity, v is the kinematic viscosity of fluid; C_S is the SGS coefficient; ∇_S is the grid size; and $S_{ij} = (\partial u_i/\partial x_j + \partial u_j/\partial x_i)/2$ is the strain rate.

2.3. Boundary conditions

For the governing equations in the present study, a complete specification of the conditions is needed at all boundaries of the solution domain. At the cell adjoining the bed and on the surface of the pier, the partial-slip condition [16] is used to replace the no-slip condition at the solid boundary. A logarithmic velocity profile is prescribed at the upstream boundary and the Neumann condition for velocity at the other boundaries is imposed. The Neumann condition for pressure is employed at all the boundaries but a prescribed pressure value is given at the downstream boundary. The free surface is modeled as a rigid-lid surface employing full-slip condition, assuming that there is no significant friction. The advantage of this assumption is that it does not require a vast amount of CPU time as free surface model [10] and it is an acceptable approximation for the case of relative large water depth considered herein.

2.4. Numerical scheme

The system represented by Equation (1) is integrated by a finite volume technique on each of the cells covering the whole domain, by invoking the mean value theorem and divergence theorem, to give

$$\frac{\partial \boldsymbol{U}_m}{\partial t} = -\frac{1}{V}\int_\Gamma \boldsymbol{H}\cdot\boldsymbol{n}\,\mathrm{d}s \tag{6}$$

where $\boldsymbol{H} = E\vec{i} + F\vec{j} + G\vec{k}$, $\boldsymbol{U}_m$ represents a mean quantity referred to the center of an element of volume V, and $\boldsymbol{n}$ is the normal vector on the surface Γ of the volume. Here $\vec{i}, \vec{j}$, and $\vec{k}$ are the unit vectors in the x-, y-, and z-directions respectively.

Equation (6) can now be discretized provided that the surface integral is approximated by the sum over the six sides of a numerical flux in the following way:

$$\frac{\partial \boldsymbol{U}_m}{\partial t} = -\frac{1}{V}\left(\sum_{r=1}^{6} \boldsymbol{H}_r\cdot\boldsymbol{s}_r\right) \tag{7}$$

where s_r are respectively the surface area vectors at the six surfaces that enclose the volume V. For the temporal integral, MacCormack's [17] explicit predictor–corrector scheme is used as follows:

predictor step:

$$\hat{U}_m^{n+1} = U_m^n - \frac{\Delta t}{V} \sum_{r=1}^{3} (H_r \cdot s_r + H_r^- \cdot s_r^-) \tag{8}$$

corrector step:

$$\hat{U}_m^{n+1} = U_m^n - \frac{\Delta t}{V} \sum_{r=1}^{3} (\hat{H}_r^+ \cdot s_r + \hat{H}_r \cdot s_r^-) \tag{9}$$

where $\wedge$ and $\hat{\wedge}$ denote the predicted and corrected values; H_r^-, H_r, and H_r^+ correspond to the flux vectors at the centers of the upstream, mid-stream, and downstream volumes respectively; s_r^- and s_r denote the surface area vectors at the upstream and downstream sides of the mid-stream volume. In Equation (8) the predictor step is backward in space. In Equation (9) the corrector step is forward in space. MacCormack [17] also showed that the two-step scheme is of second-order accuracy in time and in space. Owing to the fact that the MacCormack scheme can be either backward or forward in both predictor and corrector steps, eight different combinations can be found for three-dimensional problems. In this study, it is arranged to rotate among the eight possibilities in the computations, in order to avoid bias generated by an eventual accumulation of errors [18].

The solution at the next time level becomes

$$U_m^{n+1} = \frac{1}{2} (\hat{U}_m^{n+1} + \hat{U}_m^{n+1}) \tag{10}$$

3. MODEL VALIDATION

For verification of the numerical model, the flow and sediment conditions employed in the simulation are the same as those in the experiments for a circular pier by Dargahi [13]. They are: $u^*/u_c^* = 0.85$; $h_0/D = 1.33$; $D/d_{50} = 416.67$; $u_0 = 0.26$ m s^{-1}; and $D = 0.15$ m. Here, u^* is the bed shear velocity; u_c^* is the critical bed shear velocity for incipient motion of the sediment size d_{50}; h_0 is the inflow water depth; u_0 is the average velocity of inflow; and D is the pier diameter. The Reynolds number based on the cylinder diameter and the mean approach velocity is $Re_D = 39000$.

The computational domain is $12.5D \times 7D \times 1.33D$ (corresponding to length $\times$ width $\times$ depth). Several mesh sizes were tried to test the accuracy of the numerical scheme and search for an accurate and economical grid system. Finally it was found that a relatively coarse mesh of $76 \times 39 \times 18$ cells, as shown in Figure 1, was good enough to resolve the flow field without causing a significant numerical error. The grid system was generated by a Poisson grid generator as described by Tseng [10].
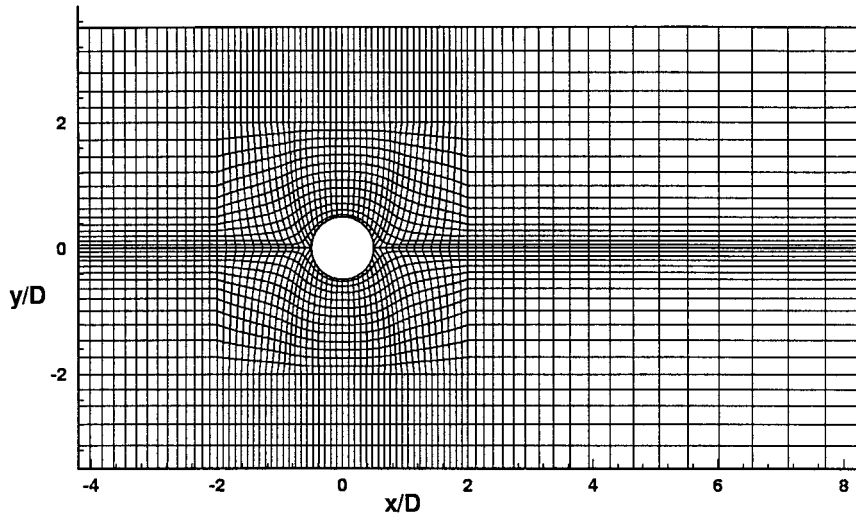
Figure 1. Grid system for circular pier.

By using the proposed method, the simulation has been carried out for the turbulent flow field around a circular pier on a rigid flat bed. Shown in Figure 2 are the variations of the drag coefficient C_D and the lift coefficient C_L obtained from simulation results. The mean C_D value
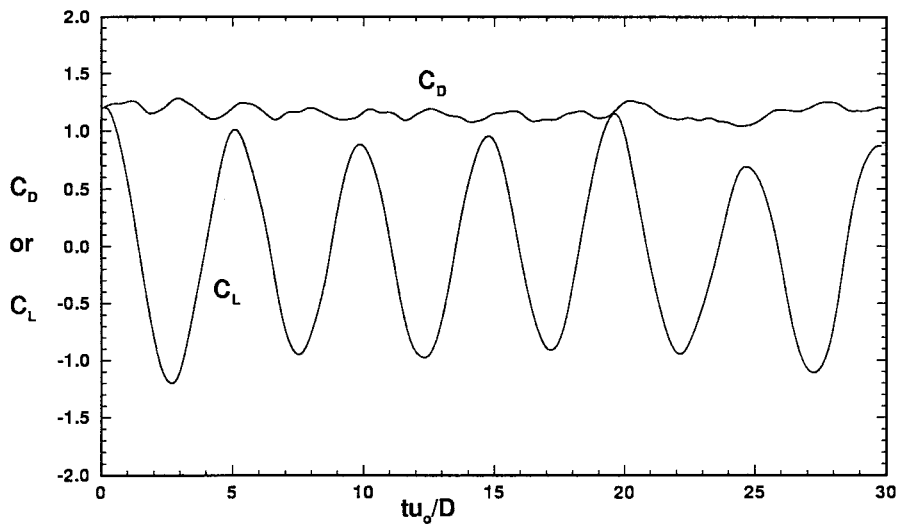

Figure 2. Variations of C_D and C_L.

is 1.155, which is very close to the 1.15 of Dargahi's experiment and the mean C_L value vanishes. The shedding frequency of the wake vortex is approximately 0.34 Hz by spectrum analysis of the data in Figure 2. This is very close to the 0.32 Hz of Dargahi's experiment.

Shown in Figure 3 are the simulated and measured results of pressure coefficient C_p along the central vertical line near the upstream face of the pier, at $x/D = -0.59$. These results imply that a downflow can be generated due to the vertical pressure gradient, and the position of maximum downflow velocity is near the bed. The agreement between the simulated and experimental results is reasonably good in Figure 3 except near the free surface, where the simulated C_p is higher than the experimental one. This overpredicted pressure distribution may be due to the rigid-lid approximation, which was employed to replace the free surface. Figure 4 illustrates the variation of near bed (at $z/D = 0.013$) pressure coefficient C_p along the line of symmetry. A strong adverse pressure gradient in front of the pier can be seen in the figure. In the region of $-1.2 < x/D < -0.9$, the C_p distribution exhibits a more or less constant value. A similar phenomenon also appears in the experimental data in the region of $-0.9 < x/D < -0.7$. The existence of this plateau in both simulated and measured results may be attributed to the effect of the horseshoe vortex, which can induce a low pressure region.

Shown in Figure 5 is the shear stress ratio τ_b/τ_m near the bed surface at $z/D = 0.013$. From the figure one can see that the mean shear stress τ_m position at station $x/D = -2.5$ (i.e., $\tau_b/\tau_m = 1$), and a reverse flow occurs in the upstream area near the pier (i.e., $-1.1 < x/D < -0.5$). The minimum value of τ_b/τ_m is reached at the point $x/D = -0.7$. This reverse flow is an indication of the phenomenon of horseshoe vortex.

Figure 6 illustrates the intensity of turbulent shear stress fluctuation defined as $\sqrt{\overline{\tau_b'^2}}/\tau_m$ near the bed surface. Here τ_b' is the fluctuation component of turbulent shear stress. As the pier is
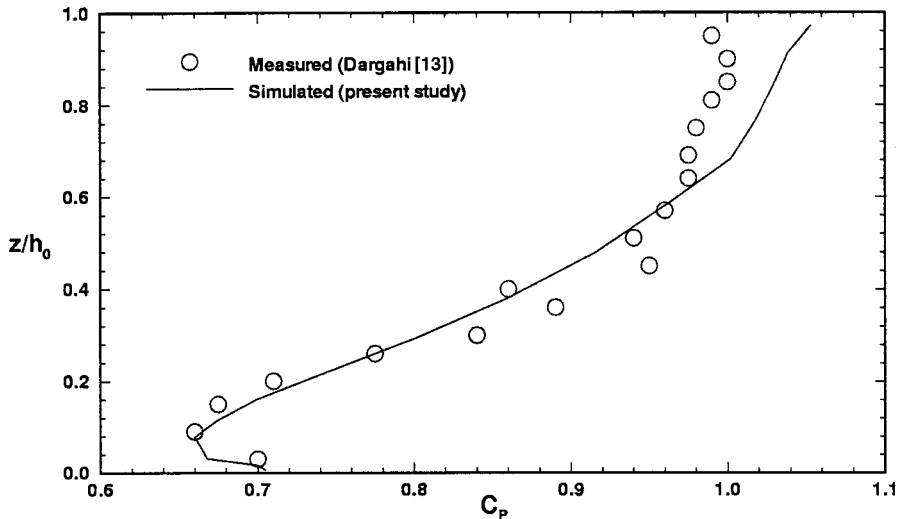

Figure 3. Variation of C_p along the central vertical near the front face of the pier.
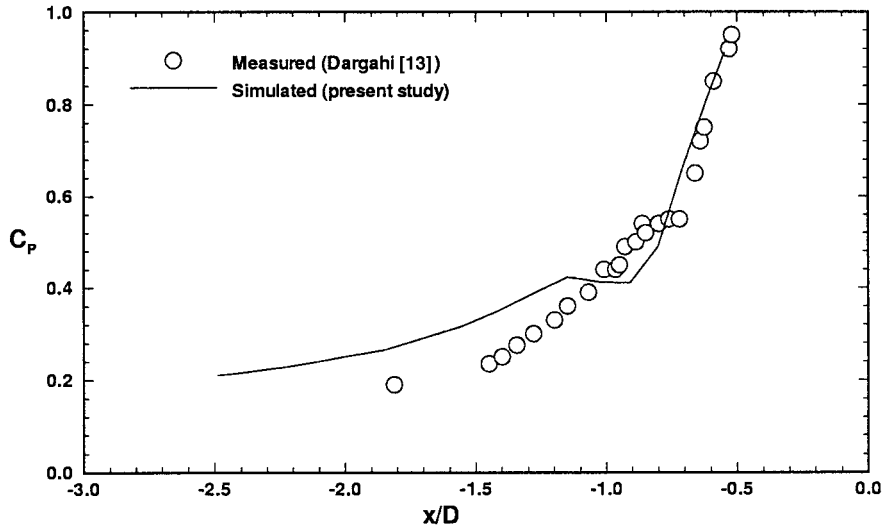
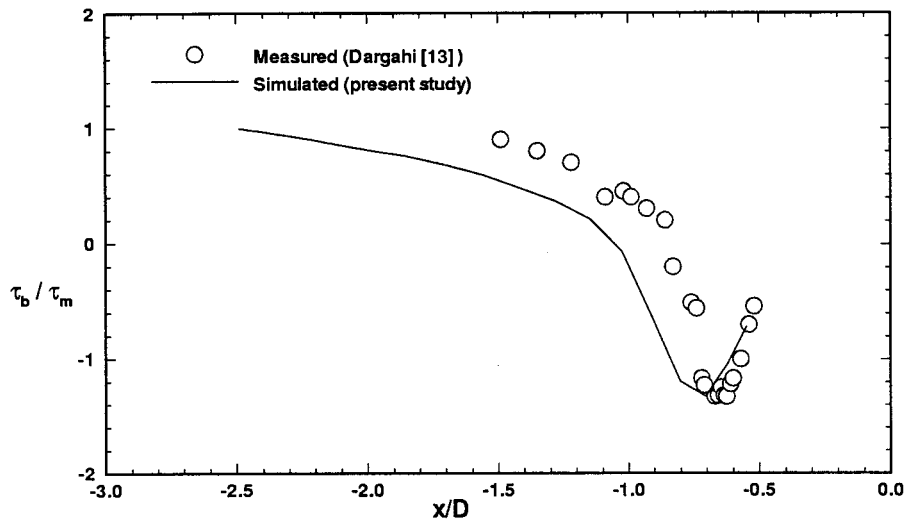Figure 4. Variation of C_p near the bed along the line of symmetry.

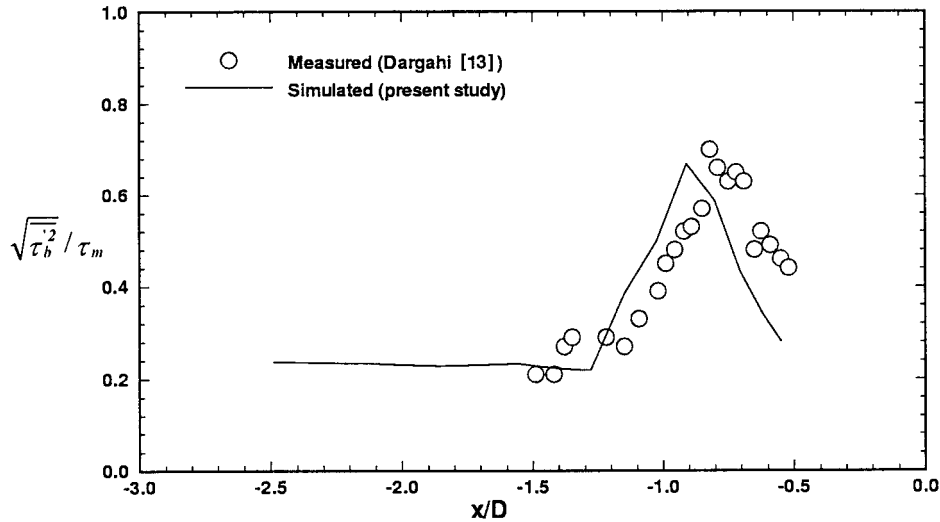Figure 5. Shear stress ratio τ_b/τ_m near the bed surface.

Figure 6. Intensity of shear stress fluctuation $\sqrt{\overline{\tau_b'^2}}/\tau_m$ near the bed surface.

approached, the distribution of the turbulent shear intensity increases until a maximum value within the reverse flow region. In the region $-1.2 < x/D < -0.5$, the turbulent intensity is considerably higher than that in the approaching flow. This circumstance is also an indication of the phenomenon of horseshoe vortex.

By comparing the simulated results with Dargdhi's measurements in Figures 2–6, one can find that the general characteristics of pressure and bed shear in front of the pier are well depicted by this proposed model. Thus, the model proposed herein has the capability to simulate three-dimensional flow around piers.

4. FLOW FEATURE COMPARISON

In this section, the patterns of the vortex system around the pier and the effect of pier shape, namely square and circular, on flow characteristics are investigated by numerical simulation using the proposed model. The computational domain is $12.5b \times 7b \times 3b$ (corresponding to length $\times$ width $\times$ depth) for both square and circular piers, where b (D for circular pier) is the pier width, with a system of $69 \times 39 \times 29$ finite volume cells for the square pier and $76 \times 39 \times 29$ for the circular pier. The flow and sediment conditions employed in the simulation are: $Re_b = Re_D = 170\,400$, $u^*/u_c^* = 0.9$, $h_0/b = 3.0$, $b/d_{50} = 126.3$, $u_0 = 0.71$ m s^{-1}, and $b = D = 0.24$ m.

4.1. Lift and drag coefficients

The variations of the drag coefficient C_D and the lift coefficient C_L are shown in Figures 7 and 8 for square and circular piers respectively. The analysis of the histogram of C_L reveals that the Strouhal number is approximately 0.11 for the square pier and 0.21 for the circular pier. These values are quite close to those obtained by other investigators (Durao *et al*. [19], Gowda [20], Song and Yuan [15]), and therefore are acceptable. Obviously, the difference in Strouhal number indicates that the shedding frequency of wake vortex for the circular pier is higher than that of the square one. The drag coefficient C_D in the case of the circular pier is smaller than that of the square one, clearly indicating that the resistance to flow is less in the case of the circular pier. In the meantime, the amplitude of variation in C_L for the case of the circular pier is smaller than that for the square one, showing that oscillations in the transverse direction would be less for the circular pier because the domain of the wake flow in this case is smaller. Figures 7 and 8 also illustrate that the amplitude of variation in C_D is smaller than that in C_L for both square and circular piers, showing that piers would be more vulnerable to vibration in the transverse direction.

4.2. Pressure coefficient

Shown in Figure 9 is the near bed (at $z/b = z/D = 0.015$) pressure coefficient along the line of symmetry for both square and circular piers. A strong adverse pressure gradient in front of the
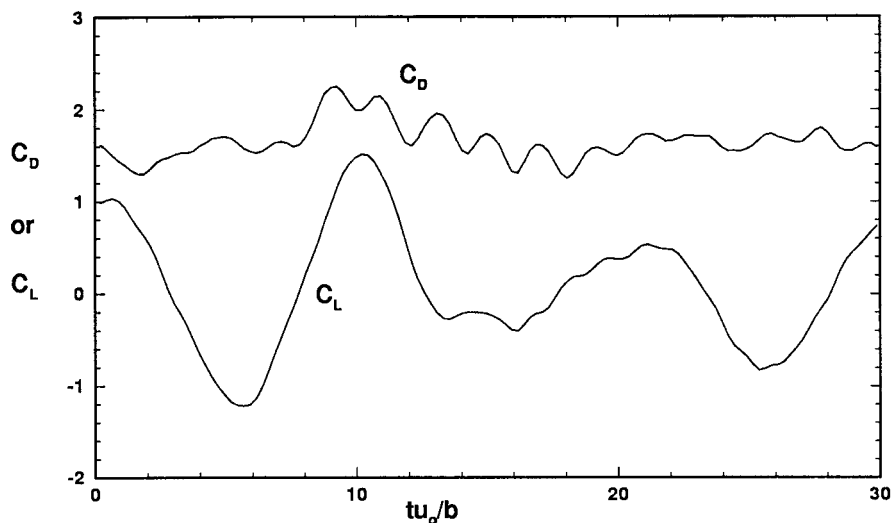

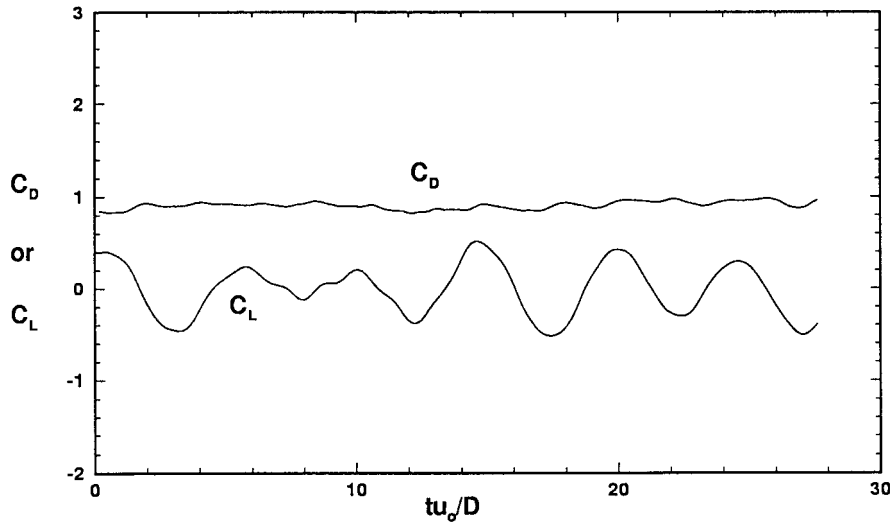Figure 7. Variations of C_D and C_L for the square pier.

Figure 8. Variations of C_D and C_L for the circular pier.

pier and a large pressure drop in the wake flow can be seen in the figure. The variation of pressure coefficient in front of the square pier is greater than that of the circular one. Figure 10 illustrates the distribution of the pressure coefficient along the central vertical line near the
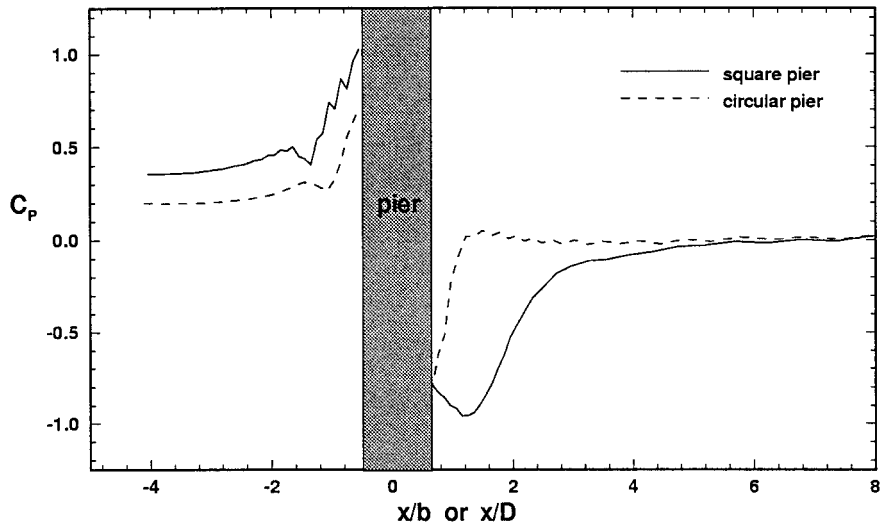

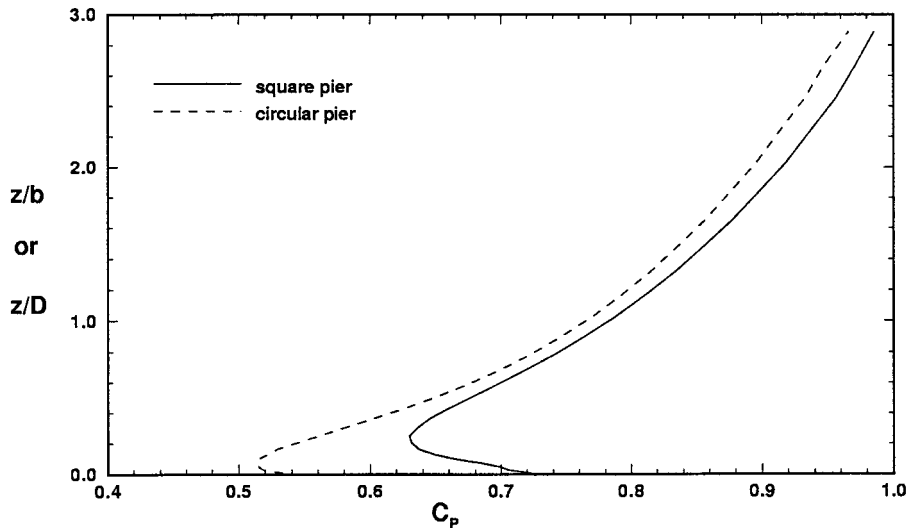Figure 9. Comparison of C_p near the bed along the line of symmetry.

Figure 10. Comparison of C_p along the central vertical near the front face of the pier.

upstream face of the piers (at $x/b = x/D = -0.6$). With these results, one can find that the pressure coefficient varies from 0.966 to 0.513 for the circular pier and from 0.985 to 0.63 for the square pier. The point of zero pressure gradient locates at $z/D = 0.07$ for the circular pier and at $z/b = 0.25$ for the square pier.

4.3. Velocity distribution

Shown in Figure 11 is the near bed (at $z/b = z/D = 0.015$) longitudinal velocity distribution along the line of symmetry for both square and circular piers. The results reveal that a reverse flow occurs in both upstream and downstream areas near the piers. The former is an indication of the phenomenon of horseshoe vortex and the latter is a combination of horseshoe vortex and wake vortex. The location of the maximum reverse velocity is closer to the pier surface in the case of circular pier. Figure 12 illustrates the downflow velocity distribution along the central vertical line near the upstream face of the pier (at $x/b = x/D = -0.6$). The result reveals that the maximum downflow velocity in the case of square pier is 33 per cent of the approach velocity, occurring at $z/b = 0.3$. In the case of circular pier, it is 21 per cent of the approach velocity, occurring at $z/D = 0.25$. By comparing Figures 10 and 12, one can find that the location of the minimum pressure coefficient is somewhat lower than that of the maximum downflow velocity for both cases.

Shown in Figure 13(a) and (b) are the mean velocity field (u, w) on the plane of symmetry of the square and circular piers respectively. The downflow velocity and horseshoe vortex upstream of the piers are clearly seen, and the upflow pattern behind the pier due to the interaction of the wake vortex and the horseshoe vortex is also obviously predicted.
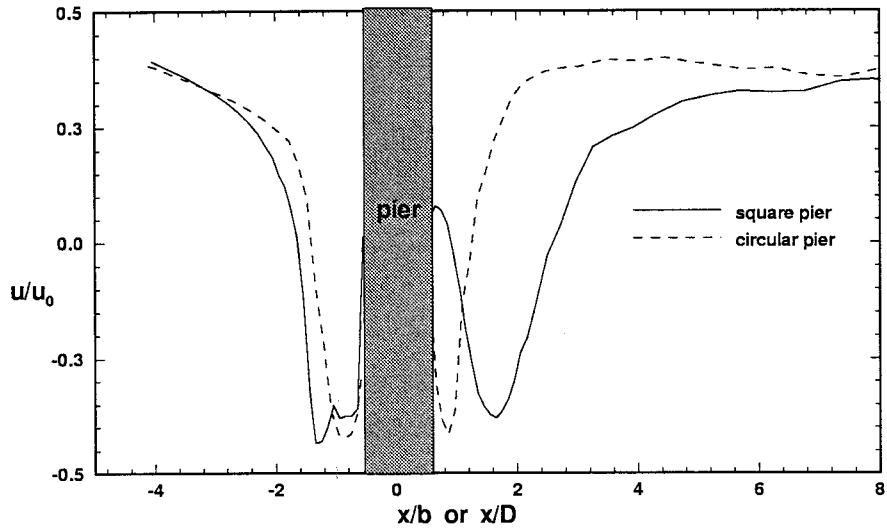
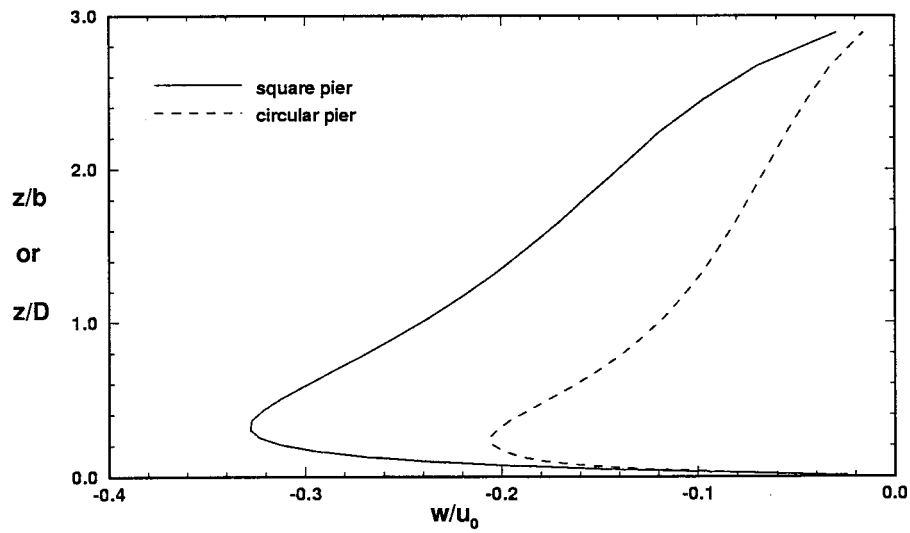Figure 11. Comparison of u/u_0 near the bed along the line of symmetry.

Figure 12. Comparison of w/u_0 along the central vertical near the front face of the pier.
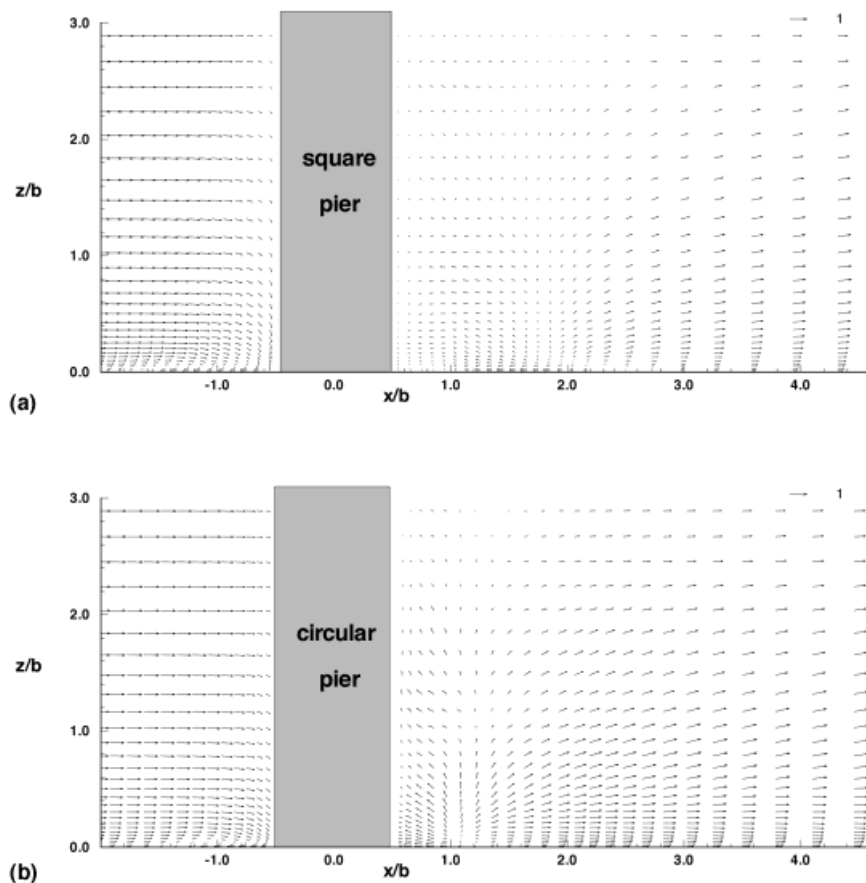
Figure 13. Mean velocity field (u, w) on the plane of symmetry. (a) Square pier, (b) circular pier.

Figure 14(a) and (b) illustrates the mean velocity field (u, v) near the channel bed (at $z/b = z/D = 0.015$) for the square and circular piers respectively. The reverse flows in upstream and downstream areas near the piers are clearly demonstrated. By comparing Figure 14(a) and (b), one can find that the velocity of reverse flows near the square pier is greater than that near the circular one, and the domains of the horseshoe vortex and the wake vortex are larger in the case of the square pier.

4.4. Vorticity distribution

Shown in Figure 15(a) and (b) is the mean vorticity component ω_x on the lower part of the $y-z$ plane, where the reverse flow velocity is the maximum in front of the square (at $x/b = -1.25$) and the circular (at $x/D = -0.86$) piers respectively. From these figures, one
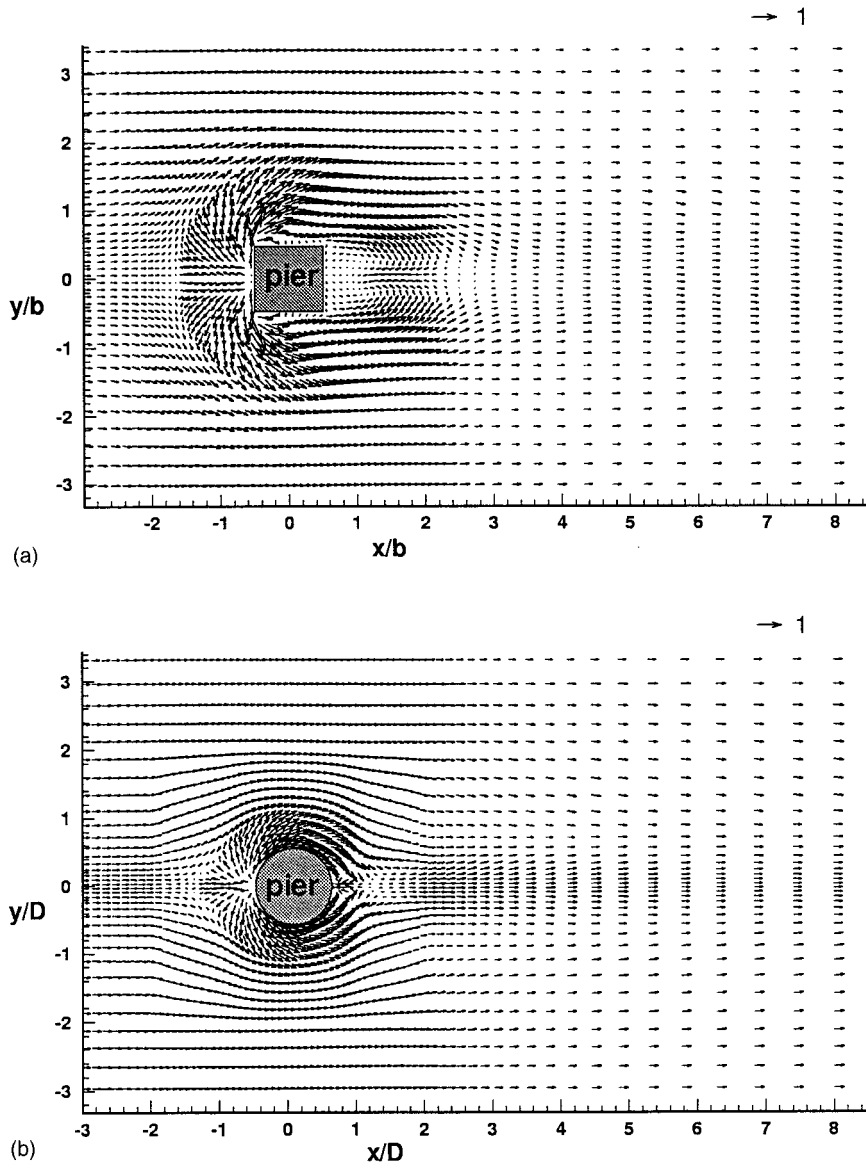
Figure 14. Mean velocity field (u, v) near the bed surface (at $z/b = z/D = 0.015$). (a) Square pier, (b) circular pier.

can find that the domain and strength of the horseshoe vortex of the square pier are greater than those of the circular one, and they both exhibit the horseshoe vortex form near the channel bed.

Figure 16(a) and (b) illustrates the mean vorticity component ω_y on the lower part of the plane of symmetry of the square and circular piers respectively. The horseshoe vortices
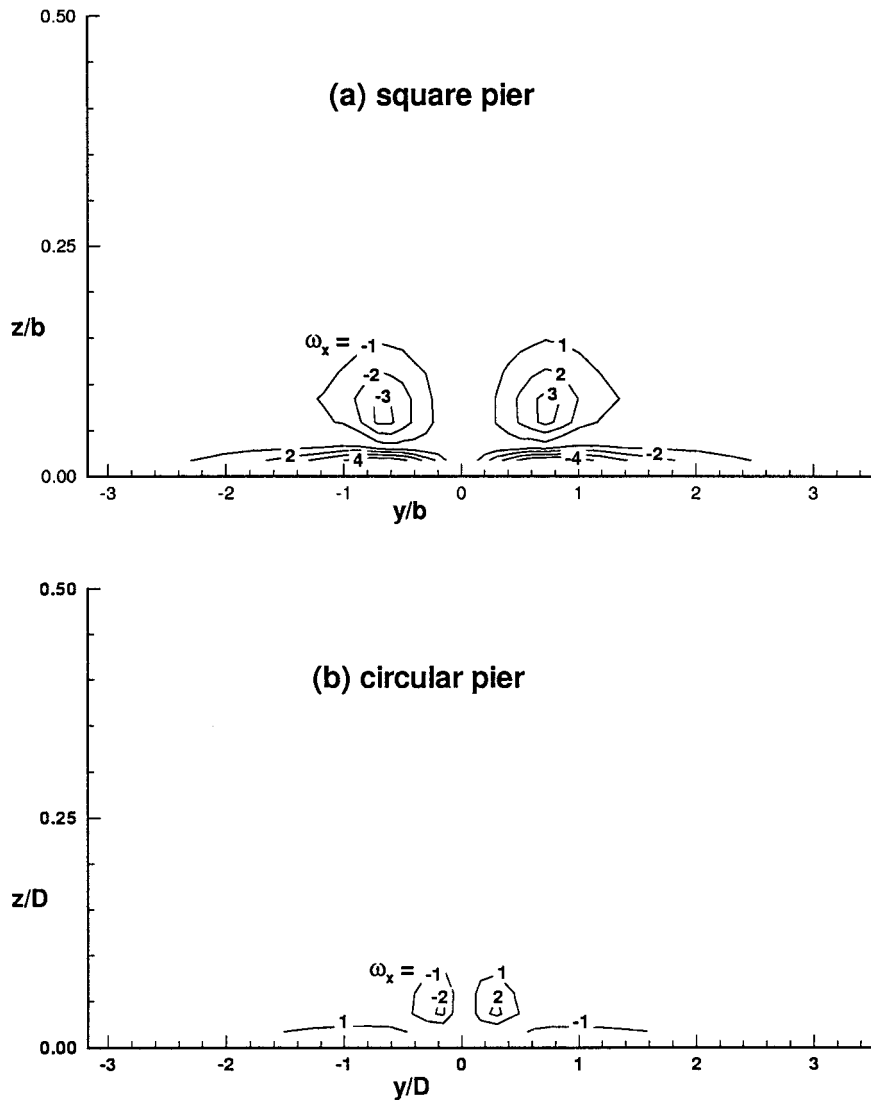
Figure 15. Mean vorticity ω_x on the y–z plane in front of the piers (at $x/b = -1.25$, $x/D = -0.86$).

(a) square pier
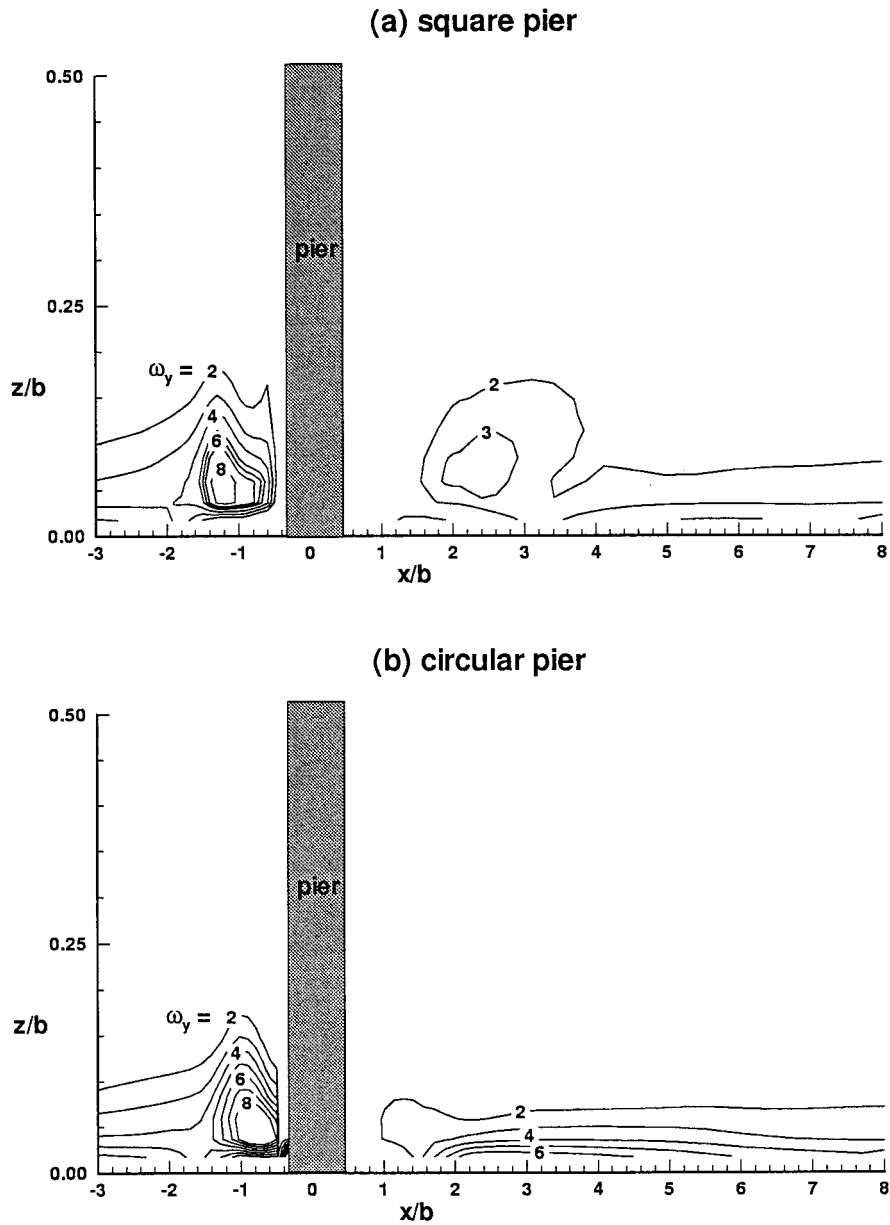

(b) circular pier

Figure 16. Mean vorticity ω_y on the plane of symmetry.

upstream of the pier are clearly seen in both cases. By comparing Figure 16(a) and (b), one can see that the axis of the horseshoe vortex in the front of the circular pier is closer to the pier than that in the case of the square one because the velocities of downflow and reverse flow generated by the circular pier are smaller than those generated by the square one.

4.5. Bed shear stress distribution

Figure 17(a) and (b) illustrates the pattern of stress ratio τ_b/τ_c near the bed surface (at $z/b = z/D = 0.015$) for square and circular piers respectively. From Figure 17(a), one can find that the maximum values of τ_b/τ_c occur at the two front corners. In Figure 17(b), one can see that the maximum values of τ_b/τ_c take place at two locations, approximately $\pm 45°$ along the surface of the circular pier. In the meantime, the area of high bed shear stress $(\tau_b/\tau_c \geq 1)$ in the case of the square pier is larger than that of the circular one.

4.6. Scouring mechanism

From the simulated results presented above, an insight into the mechanism of scouring is gained in terms of the flow field and its significance in the process of scouring. Generally speaking, the results of the numerical simulation indicate that the main features of the flow around the pier are the complex three-dimensional turbulent flow near the upstream face of the pier and the periodical vortex shedding in the downstream region. In the region of reverse flow near the upstream face, the lateral flow velocity is also developed due to the lateral pressure gradient in the direction normal to the main flow. The downflow in the front side of the pier, arising from the vertical pressure gradient, joins the reverse and lateral flow velocities to form the vortex system near the bed, which is stretched around the pier base like a horseshoe. Therefore, it can be said that the downflow is the key component in forming the horseshoe vortex. These phenomena demonstrated by the numerical simulation are in good agreement with those observed in experiments by other investigators, such as Raudkivi [5] and Dargahi [13].

From the results shown in Figure 14(a) and (b) and Figure 17(a) and (b), one can infer that the zones where scouring or deposition tend to occur on initially flat bed can be estimated by using the criteria of shear stress ratio τ_b/τ_c being greater or less than unity. By comparing Figure 17(a) and (b), one can further infer that the initial scour hole would occur near the two front corners of the square pier and near the $\pm 45°$ position of the circular pier, and that the area of the scour hole around the square pier would be greater than that of the circular one. At the same time, the downflow, which acts like a jet impinging on the bed, brings additional scouring effect. As the initial scour takes place, one can expect the bed shear ratio τ_b/τ_c to decrease and the strength of downflow to increase. Consequently, the scouring process may continue for some time until the flow field and forces acting on sediment particles are greatly modified by the scour hole. Thus, the final scour is a result of combined action of bed shear and downflow, reflecting the effect of horseshoe vortex. In other words, the horseshoe vortex is the mechanism responsible for the scour around the pier as stated by Dargahi [21].
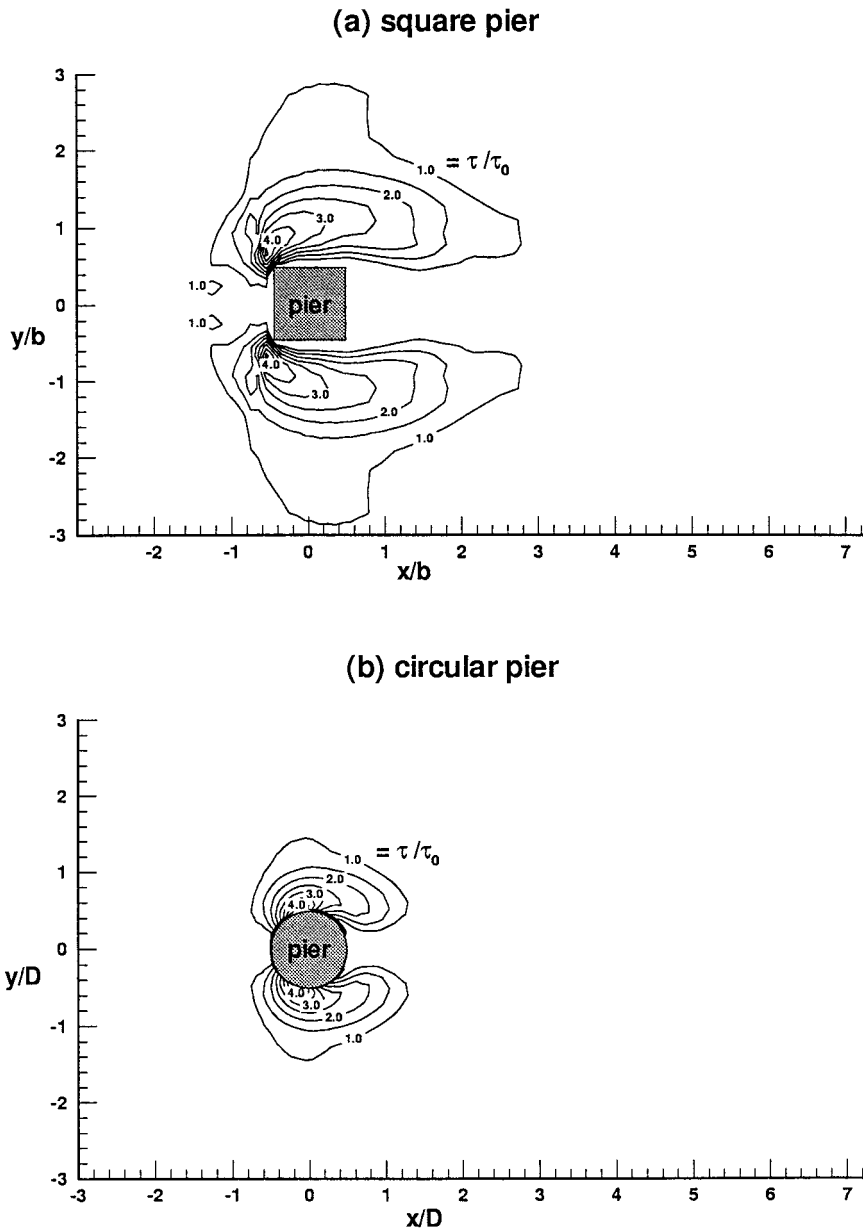
(a) square pier

(b) circular pier

Figure 17. Pattern of τ_b/τ_c near the bed surface (at $z/b = z/D = 0.015$).

5. CONCLUSIONS

From the results presented above, the following conclusions can be drawn:

1. The flow pattern of the horseshoe vortex around the pier, downflow in the front side of the pier, and the wake vortex behind the pier are all well simulated by the flow model, which employs a finite volume method based on MacCormack's explicit predictor–corrector scheme to solve weakly compressible hydrodynamic flow equations, together with Smagorinsky's SGS turbulence model.

2. The results of the numerical simulation illustrate that the main characteristics of the flow around the piers are the complex three-dimensional turbulent flow in the upstream area in front of the pier and the wake flow in the downstream region behind the pier. In the region of reverse flow near the upstream face, the lateral flow velocity is developed due to the lateral pressure gradient normal to the main flow direction and the horseshoe vortex interacts with the wake vortex to create the upflow behind the pier. The downflow near the front face of the pier joins the upstream reverse flow to form the vortex system near the bed, which is then stretched around the pier base like a horseshoe. These phenomena demonstrated by the numerical simulation are in good agreement with those observed in experiments by other investigators, e.g., Raudkivi [5], Dargahi [13].

3. In general, the flow patterns for square and circular piers are similar. However, the Strouhal number in the case of the circular pier is larger than the square one, and the vortex shedding in the wake flow for the circular pier is faster and more unstable than that for the square one. The drag coefficient in the case of circular pier is smaller than that of the square one, indicating that the resistance to flow is lower in the case of the circular pier. In the meantime, the amplitude of variation in lift coefficient in the case of the circular pier is also smaller than that of the square one, showing that oscillations in the transverse direction would be less for the circular pier. Besides, the amplitude of variation in the lift coefficient is larger than that in the drag coefficient for both square and circular piers. This implies that piers would be more vulnerable to vibration in the transverse direction.

4. From the flow feature comparison, the results also explore that the strength of the downflow (Figure 12) along a vertical line near the upstream face are greater in the case of square pier. The domains of the horseshoe vortex and the wake vortex in the case of the circular pier are smaller than those in the case of the square one (Figure 14). In the meantime, the position of the horseshoe vortex around the circular pier is closer to the front face than that around the square pier (Figure 16). In addition, the domain of high bed shear stress in the case of the square pier is greater than that of the circular one (Figure 17).

5. From the simulated results presented above, an insight into the mechanism of scouring is gained. Generally speaking, the initial scour hole would occur near the two front corners of square pier and near the $\pm 45°$ position of the circular pier, and the area of the scour hole around the square pier would be greater than that around the circular one. At the same time, the downflow, which acts like a jet impinging on the bed, brings additional scouring effect. As the initial scour takes place, one can expect the bed shear ratio τ_b/τ_c to decrease and the strength of the downflow to increase. Consequently, the scouring process

may continue for some time until the flow field and forces acting on sediment particles are greatly modified by the scour hole. Thus, the final scour is a result of combined action of bed shear and downflow, reflecting the effect of the horseshoe vortex. In other words, the horseshoe vortex is the mechanism responsible for the scour around the pier as stated by Dargahi [21].

REFERENCES

1. Breusers HNC, Nicollet G, Shen HW. Local scour around cylindrical piers. *Journal of Hydraulic Research* 1977; **15**: 211–252.
2. Ettema R. Scour at bridge piers. Report No. 216, University of Auckland, Auckland, New Zealand, 1980.
3. Raudkivi J, Ettema R. Clear-water scour at cylindrical piers. *Journal of Hydraulic Engineering*, ASCE 1983; **109**(3): 338–359.
4. Raudkivi AJ. Functional trends of scour at bridge piers. *Journal of Hydraulic Engineering*, ASCE 1986; **112**(1): 1–13.
5. Melville BW, Sutherland AJ. Design method for local scour at bridge piers. *Journal of Hydraulic Engineering*, ASCE 1988; **114**(10): 1210–1226.
6. Olsen NRB, Melaaen MC. Three-dimensional calculation of scour around cylinders. *Journal of Hydraulic Engineering*, ASCE 1993; **119**(9): 1048–1054.
7. Richardson JE, Panchang VG. Three-dimensional simulation of scour-inducing flow at bridge piers. *Journal of Hydraulic Engineering*, ASCE 1998; **124**(5): 530–540.
8. Olsen NRB, Kjellesvig HM. Three-dimensional numerical flow modeling for estimation of maximum local scour depth. *Journal of Hydraulic Research* 1998; **36**(4): 579–590.
9. Yen CL, Song CS, Tseng MH. Numerical simulation of flow and scour around bridge pier (I). Research Report, National Science Council, Taipei, ROC (in Chinese), 1993.
10. Tseng MH. Numerical simulation of 3D flow and scour around bridge pier. PhD Dissertation, Department of Civil Engineering, National Taiwan University (in Chinese), 1994.
11. Yen CL, Song CS, Tseng MH. Numerical simulation of flow and scour around a square pier. In *9th Congress of APD-IAHR*, Cheong HF, Shanker NJ, Chan ES, Ng WJ (eds). Econ Piling Pte Ltd: Singapore, 1994; 368–375.
12. Smagorinsky J. General circulation experiments with primitive equation. *Monthly Weather Review* 1963; **91**(3): 99–154.
13. Dargahi B. The turbulent flow field around a circular cylinder. *Experiments in Fluids* 1989; **8**: 1–12.
14. Song C, Yuan M. A weakly compressible flow model and rapid convergence method. *Journal of Fluids Engineering*, ASME 1988; **110**: 441–445.
15. Song C, Yuan M. Simulations of vortex-shedding flow about a circular cylinder at high Reynolds numbers. *Journal of Fluids Engineering*, ASME 1990; **112**: 155–161.
16. Yuan M, Song C, He J. Numerical analysis of turbulent flow in a two-dimensional nonsymmetric plane-wall diffuser. *Journal of Fluids Engineering*, ASME 1991; **113**: 210–215.
17. MacCormack RW. The effect of viscosity in hypervelocity impact cratering. AIAA Paper 69-354, 1969.
18. Hirsch C. *Numerical Computation of Internal and External Flows*, vol. 2. Wiley: New York, 1988.
19. Durao DFG, Heitor MV, Pereira JCF. Measurements of turbulent and periodic flows around a square cross-section cylinder. *Experiments in Fluids* 1988; **6**: 298–304.
20. Gowda BHL. Some measurements of the phenomena of vortex shedding and induced vibrations of circular cylinder. Technische Universitat Berlin Report, DLR-FB 75-01, 1975.
21. Dargahi B. Controlling mechanism of local scouring. *Journal of Hydraulic Engineering*, ASCE 1990; **116**(10): 1197–1214.